

WellPINN: Accurate Well Representation for Transient Fluid Pressure Diffusion in Subsurface Reservoirs with Physics-Informed Neural Networks

Linus Walter^{*1,2}, Qingkai Kong³, Sara Hanson-Hedgecock¹, and Víctor Vilarrasa^{†1}

¹Global Change Research Group (GCRG), IMEDEA, CSIC-UIB, Spain

²Department of Civil and Environmental Engineering (DECA), Universitat Politècnica de Catalunya·BarcelonaTech (UPC), Barcelona, Spain

³Lawrence Livermore National Laboratory, Livermore, USA

July 15, 2025

Keypoints:

- WellPINN is a sequential training workflow using physics-informed neural networks (PINNs) that solve transient fluid flow problems
- We accurately represent a well at a reservoir-scale domain spanning three order of magnitude in space dimension
- Domain decomposition and logarithmic scaling of time is required to accurately represent wells with PINNs that use tanh activation functions

Abstract

Accurate representation of wells is essential for reliable reservoir characterization and simulation of operational scenarios in subsurface flow models. Physics-informed neural networks (PINNs) have recently emerged as a promising method for reservoir modeling, offering seamless integration of monitoring data and governing physical equations. However, existing PINN-based studies face major challenges in capturing fluid pressure near wells, particularly during the early stage after injection begins. To address this, we propose WellPINN, a modeling workflow that combines the outputs of multiple sequentially trained PINN models to accurately represent wells. This workflow iteratively approximates the radius of the equivalent well to match the actual well dimensions by decomposing the domain into stepwise shrinking subdomains with a simultaneously reducing equivalent well radius. Our results demonstrate that sequential training of superimposing networks around the pumping well is the first workflow that focuses on accurate inference of fluid pressure from pumping rates throughout the entire injection period, significantly advancing the potential of PINNs for inverse modeling and operational scenario simulations. All data and code for this paper will be made openly available at <https://github.com/linuswalter/WellPINN>.

^{*}Corresponding author: linus.walter@csic.es

[†]Co-Corresponding author: victor.vilarrasa@csic.es

Plain Language Summary

Accurately representing wells is crucial when building reservoir models to simulate fluid flow. During well testing, it is particularly important to match applied flow rates and observed pressures to calibrate the model. A promising tool are physics-informed neural networks (PINNs) that flexibly combine measured data with physical laws. However, existing PINNs often fail to capture the fluid pressure field near wells, especially immediately after injection begins. To overcome this limitation, we developed a new workflow called WellPINN. It uses several PINN models in sequence. The first model is trained for the whole modeling domain, while each subsequent model focuses on a smaller area around the well. Simultaneously, we also reduce the dimensions of the representative well. We demonstrate WellPINN on a test case involving a single pumping well in a two-dimensional reservoir. Our results show that using three PINNs in sequence can successfully model pressure changes from the reservoir boundary to the well center across multiple spatial scales. WellPINN is the first PINN-based method to accurately predict pressure throughout the entire injection period. This opens new possibilities for applying PINNs in inverse modeling and planning real-world reservoir operations, including in more complex reservoir settings or with multiple wells.

1 Introduction

Wells are fundamental for hydrogeological applications such as drinking water production, aquifer remediation, and harnessing of geothermal energy (Hölting and Coldewey, 2013). During the exploration phase, well tests help characterize subsurface parameters (Slotte and Berg, 2017; Vaezi et al., 2024; Watson et al., 1994), while later stages require simulations of fluid pressure responses to operational scenarios (Bentley, 2020). These simulations use forward models to estimate the spatiotemporal distribution of fluid pressure $p(\mathbf{x}, t)$ in response to injection and/or pumping flow rates q_w . State-of-the-art for reservoir modeling are numerical solvers like ‘MOOSE Framework’ (Giudicelli et al., 2024), ‘OpenGeoSys’ (Naumov et al., 2022), ‘CODE_BRIGHT’ (Olivella et al., 2023), and ‘GEOS’ (Castelletto et al., 2024), which solve conservation equations of mass, energy, and momentum using finite element, difference, or volume methods (Bentley, 2020). These methods discretize the geological domain with meshes that are refined around wells to resolve steep pressure gradients. Such models are effective for simulations, but they often struggle to incorporate noisy field data and quantify uncertainties. A potential alternative could be data-driven machine learning approaches that flexibly integrate data (Sun et al., 2022), but typically require more data than subsurface systems can provide (Shen et al., 2023).

To overcome these limitations, hybrid models, such as physics-informed neural networks (PINNs) (Lagaris et al., 1998; Raissi et al., 2019) and theory-guided networks (TgNNs) (Karpatne et al., 2017), combine the strengths of physics-based and data-driven models by embedding residuals of the governing partial differential equations (PDEs) into the loss function via automatic differentiation (Baydin et al., 2015). PINNs have shown potential across disciplines (Karniadakis et al., 2021), supported by recent advances in loss weighting (Wang, Sankaran, et al., 2023), activation function optimization (Abbasi and Andersen, 2023; Huang and Alkhalifah, 2023), and hard constraints (Sukumar and Srivastava, 2022; Taufik et al., 2024). In geosciences, PINNs are increasingly used in reservoir modeling. Recent developments include multiphysics coupling (Haghighat, Amini, and Juanes, 2021), two-phase flow (Hanna et al., 2022), sharp material transitions (Lehmann et al., 2023; Sarma et al., 2024), and fractured domains (Abbasi, Moseley, et al., 2025; Yan et al., 2024). Despite these advances, model simplifications such as homogeneous materials (Haghighat, Amini, and Juanes, 2021), stationary flow (Lehmann et al., 2023), or dense grids of observation points (Tartakovsky et al., 2020; Wang, Zhang, et al., 2020) remain common, reflecting the ongoing challenges in adapting PINNs for practical

reservoir modeling.

Apart from these idealizations, a major challenge for PINNs is accurate well representation in the reservoir model. Analytical solutions represent singularities like wells as point sources. This representation is not suitable for PINNs because Artificial Neural Networks (ANNs) perform best on smooth, continuous, similarly scaled variables (Rumelhart et al., 1986). Therefore, most studies represent wells in PINNs with equivalent well functions to smoothen steep pressure gradients in the vicinity of the well (Cuomo et al., 2023; Huang, Liu, et al., 2021; Liu, Li, et al., 2024; Soriano et al., 2021; Teng et al., 2022; Wang, Kong, and Zhang, 2024; Zhang et al., 2022).

A common equivalent well representation is the Gaussian function, whose integral always equals one and which is directly derivable (Huang, Liu, et al., 2021; Teng et al., 2022). In addition, Cuomo et al. (2023) compared the model performance of a piecewise cubic function to a cosine function, with a better performance for the latter one. Liu, Li, et al. (2024) obtained good results for well representation with a Lorentz function, although it requires a numerical method for integral calculation. Other levels of complexity are added by the use of multiple injection wells (Cuomo et al., 2023; Liu, Li, et al., 2024; Zhang et al., 2022) or a heterogeneous modeling domain (Liu, Li, et al., 2024). Incorporating hard constraints effectively improves model convergence by reducing the number of loss terms (Zhang et al., 2022) and also domain decomposition produces more accurate results (Teng et al., 2022). A major advancement is the implementation of Wang, Kong, and Zhang (2024) that provided a complex inversion workflow for the estimation of the permeability field based on a physics-informed deep convolutional encoder-decoder network that infers the evolution of the pore pressure field $p(\mathbf{x}, t)$ by using multiple wells and a range of observation points, also at the location of the well. The use of observation points for fluid pressure within the modeling domain is common among several studies (Wang, Kong, and Zhang, 2024; Zhang et al., 2022). However, we are concerned that the number of incorporated observations exceeds the usually available number of observations in the field, especially for deep subsurface projects due to the high drilling cost (Beckers and McCabe, 2019). Although these studies demonstrate the general suitability of equivalent well functions, they often require a relatively large equivalent well radius, typically at least 10 % of the domain size, to achieve stable convergence (Cuomo et al., 2023; Liu, Li, et al., 2024; Teng et al., 2022; Zhang et al., 2022). Although this is sufficient to capture $p(\mathbf{x}, t)$ in the far field for late injection times, these approaches underestimate the well pressure p_w by up to 30% during late injection times and completely miss early-time diffusion. This limitation reduces the reliability of the model for history matching based on q_w . These limitations motivate the need for a PINN workflow capable of capturing a realistic representation of the well with sparse data.

We introduce ‘WellPINN’ to address the limited well representation capabilities of previous studies by proposing a sequential training workflow that combines multiple PINN models. We subdivide the modeling domain into nested subdomains, with each inner model refining the solution near the well using the equivalent radius of the previously trained model as its new boundary. We first train a PINN across the entire domain, providing a function $\hat{p}(\mathbf{x}, t)$ that captures $p(\mathbf{x}, t)$ in the far field, but remains inaccurate near the well. Subsequently, trained PINNs focus on smaller subdomains, progressively refining the pressure field near the well by using smaller equivalent well radii. We apply the WellPINN workflow to a two-dimensional modeling domain with a single injection well of radius $r = 10 \text{ cm}$, located at the center of a 100 m by side square. Our results show an accurate inference of p_w throughout the entire injection period, including early injection times. By isolating the partial derivative terms for each PINN model, we ensure consistent training times and avoid accumulating computational overhead by iteratively increasing the number of PINN functions. Thus, our approach offers a scalable solution to the multiscale challenge of well representation in a large domain, posing an important step for future applications of PINNs in history matching of pumping well tests.

2 WellPINN: A Sequential Modeling Workflow for Well Representation with PINN

This study addresses the transient diffusion of fluid pressure $p(x, y, t)$ in a 2D domain with a special focus on accurately representing a single well, as shown schematically in Figure 1a. The governing equation for $p(x, y, t)$ reads

$$0 = S_s \frac{\partial p(x, y, t)}{\partial t} - \text{div} (\mathbf{K}(x, y) \text{grad } p(x, y, t)) - \rho g f(x, y, t), \quad (1)$$

where $\mathbf{K}(x, y)$ is the hydraulic conductivity field, S_s is the specific storage coefficient, x and y are the Cartesian coordinates, t is time, and $f(x, y, t)$ is a source/sink term per unit volume representing the well. The gravity term is neglected in our case because gravity g is oriented perpendicular to our reservoir plane. We first introduce the relationship $K(x, y) = k(x, y) \frac{\rho \times g}{\mu}$, where ρ is fluid density and μ is fluid viscosity, and replace the specific storage S_s with its equivalent pressure formulation $S_s = S'_s \rho g$. Then we cancel ρ and g in both terms and get

$$0 = S'_s \frac{\partial p}{\partial t} - \frac{1}{\mu} \text{div} (k(x, y) \text{grad } p) - f(x, y, t). \quad (2)$$

We determine S'_s from the definition for uniaxial specific storage as $S'_s = \phi \kappa_R^f + (\alpha_B - \phi) \kappa_R^s$ where ϕ is porosity, κ_R^f is the bulk modulus of the fluid (Wang, 2000). The source term $f(x, y, t)$ writes as

$$f(x, y, t) = \frac{Q}{d} \frac{1}{2\pi \sigma^2} \exp \left(-\frac{0.5}{\sigma^2} ((x - x_0)^2 + (y - y_0)^2) \right), \quad (3)$$

where d is the thickness of the reservoir, assumed as unity in the 2D model. The assigned values for the material parameters in Equation (2) and Equation (3) are summarized in Table 1. We introduce the following dimensionless parameters for the independent variables of space x, y and time t as well as for the dependent variables pressure $p(x, y, t)$, permeability $k(x, y)$ and the source term $f(x, y, t)$

$$\bar{x} = \frac{x}{x_c} \quad \bar{y} = \frac{y}{y_c} \quad \bar{t} = \frac{t}{t_c}$$

$$\bar{p}(\bar{x}, \bar{y}, \bar{t}) = \frac{p(x, y, t)}{p_c} \quad \bar{k}(\bar{x}, \bar{y}) = \frac{k(x, y)}{k_c} \quad \bar{f}(\bar{x}, \bar{y}, \bar{t}) = \frac{f(x, y, t)}{f_c}.$$

We assume that $y_c = x_c$ and replace each dimensional variable n with the respective dimensionless \bar{n} , denoted by a bar, and characteristic counterpart n_c , denoted by the subscript c , in Equation (2), resulting in

$$0 = S'_s \frac{p_c}{t_c} \frac{\bar{\partial} \bar{p}}{\bar{\partial} \bar{t}} - \frac{k_c p_c}{\mu x_c^2} \text{div} (\bar{k} \text{grad } \bar{p}) - f_c \bar{f}(\bar{x}, \bar{y}, \bar{t})$$

$$0 = \underbrace{S'_s \frac{x_c^2 \mu}{k_c t_c}}_{=1} \frac{\bar{\partial} \bar{p}}{\bar{\partial} \bar{t}} - \text{div} (\bar{k} \text{grad } \bar{p}) - \underbrace{\frac{x_c^2 \mu f_c}{k_c p_c}}_{=1} \bar{f}(\bar{x}, \bar{y}, \bar{t}).$$

The factors in the first term, A , and the third term, B , are assumed to be equal to one to maintain the order unity (Langtangen and Pedersen, 2016).

We choose the parameters f_c , p_c and k_c by their maximum parameters

$$\begin{aligned} x_c &= 1 \text{ m} \\ k_c &= k_{\max} \\ f_c &= Q_{\max} \frac{1}{1 \text{ m}} \frac{1}{1 \text{ m}^2} e^0 \quad [\text{s}^{-1}], \end{aligned}$$

where we assume $\sigma^2 = 1/2\pi$ (see Equation (3)).

Therefore, we choose the remaining variables as the following:

$$p_c = \frac{x_c^2 f_c \mu}{k_c} \quad t_c = \frac{x_c^2 S_s \mu}{k_c}$$

The dimensionless form of Equation (1) reads therefore as

$$R = \frac{\partial \hat{p}(\bar{x}, \bar{y}, \bar{t}; \theta)}{\partial \bar{t}} - \overline{\text{div}} (\overline{\text{grad}} \hat{p}(\bar{x}, \bar{y}, \bar{t}; \theta)) - \bar{f}(\bar{x}, \bar{y}, \bar{t}), \quad (4)$$

In addition to the dimensionless formulation, we represent the source/sink term similarly to Teng et al. (2022) and Zhang et al. (2022) with a bi-variate formulation of the Gaussian function as

$$\bar{f}(\bar{x}, \bar{y}) = \frac{1}{2\pi \sigma^2} \times \exp \left(-\frac{(\bar{x} - \mu_x)^2 + (\bar{y} - \mu_y)^2}{2\sigma^2} \right), \quad (5)$$

where μ_x and μ_y represent the location of the well within the domain.

We infer the dimensionless ground truth $\bar{p}(\bar{x}, \bar{y}, \bar{t})$ using an ANN $\hat{p}(\bar{x}, \bar{y}, \bar{t}; \theta)$, where $\hat{\cdot}$ denotes the ANN output, based on the multilayer perceptron (Minsky and Papert, 1969; Rumelhart et al., 1986), following the PINN framework (Lagaris et al., 1998; Raissi et al., 2019). As shown in Figure 1b, the PINN receives three dimensionless input variables \bar{x} , \bar{y} , and \bar{t} . Before being passed to the network, the spatial dimensions \bar{x} and \bar{y} are scaled with a min-max scaler, while time \bar{t} is log-scaled to account for the early-time nonlinearity in pressure diffusion. Due to smooth activation functions, $\hat{p}(\bar{x}, \bar{y}, \bar{t}; \theta)$ is continuous and therefore differentiable at all collocation points $\{x_{\text{cp}}^i, y_{\text{cp}}^i, t_{\text{cp}}^i, p_{\text{cp}}^i\}_{i=1}^{N_{\text{cp}}}$ by using automatic differentiation (Baydin et al., 2015). Next, we compute the residual R of Equation (4) and define the PINN loss as

$$\mathcal{L} = \mathcal{L}_{\text{pde}} = \text{RMSE}(R), \quad (6)$$

where the PDE loss \mathcal{L}_{pde} is the root mean squared error (RMSE) of R (Raissi et al., 2019). The optimizer adjusts the weights and biases of the network to minimize \mathcal{L} during training.

As Equation (6) indicates, we use only one loss term in our workflow. That is because we do not use any observations of $\bar{p}(\bar{x}, \bar{y}, \bar{t})$ for the model training, which would otherwise facilitate the training process. Secondly, we incorporate all additional constraints, such as boundary conditions and initial conditions, directly into a composite pressure function $\hat{p}_c(\bar{x}, \bar{y}, \bar{t}; \theta)$ that is written as

$$\hat{p}_c(\bar{x}, \bar{y}, \bar{t}; \theta) = \hat{p}(\bar{x}, \bar{y}, \bar{t}; \theta) \times \tau(\bar{x}, \bar{y}, \bar{t}), \quad (7)$$

where $\tau(\bar{x}, \bar{y}, \bar{t})$ is a piecewise approximate distance function. We adopt $\tau(\bar{x}, \bar{y}, \bar{t})$ from Sukumar and Srivastava (2022) and implement it as a hard constraint for our PINN model similar to Lu et al. (2021), Roy and Castonguay (2024), Lai et al. (2023), and Zhang et al. (2022) as

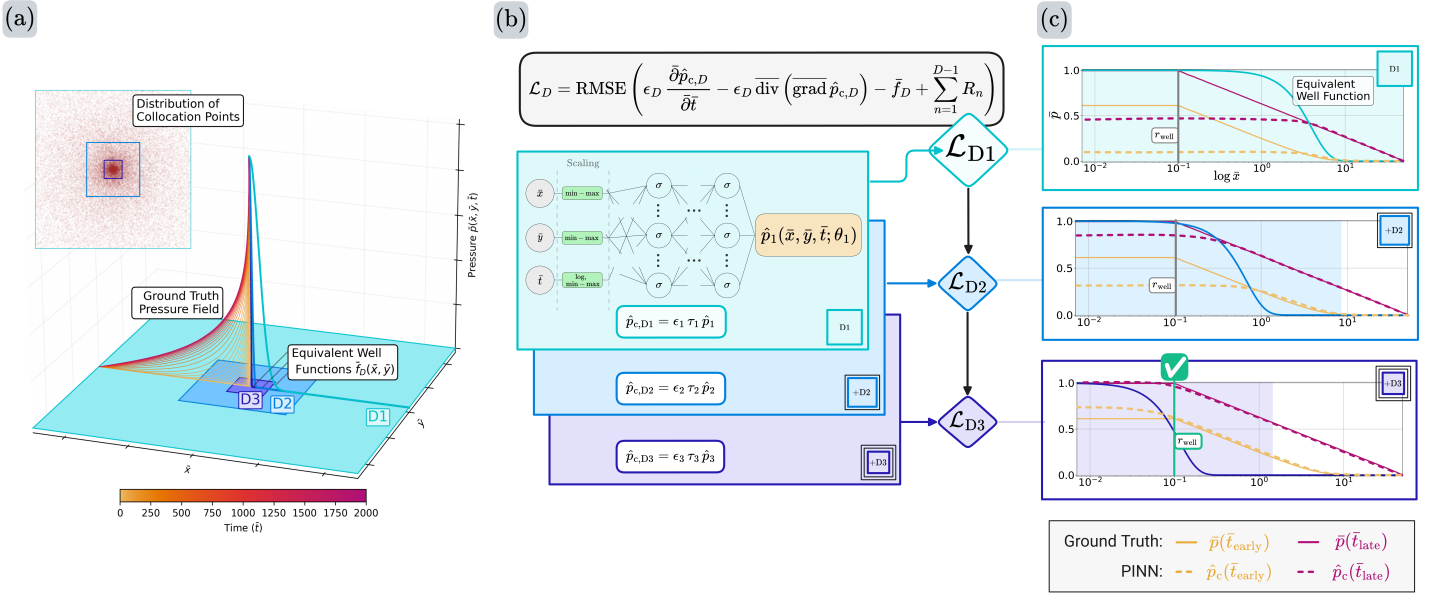


Figure 1 Sequential training workflow of our PINN model for transient fluid pressure diffusion from a single well in a 2D domain. (a) Ground truth solution illustrating the diffusion of fluid pressure $\bar{p}(\bar{x}, \bar{y}, \bar{t})$ from the injection well. The domain is decomposed into subdomains D1 (light blue), D2 (blue), and D3 (dark purple), with each assigned an equivalent well function $\bar{f}_D(\bar{x}, \bar{y})$. Collocation points are concentrated near the well (inset). (b) Schematic workflow of the training process showing the composite pressure solution $\hat{p}_{c,D}$ for each subdomain, constructed from the neural network output \hat{p}_D , weighting factor ϵ_D , and a hard constraining approximate distance function τ_D . The training of $\hat{p}_{c,D}$ is guided by the loss function \mathcal{L}_D . (c) In D1, the model \hat{p}_c infers the ground truth up to the equivalent well radius \bar{r}_{weq} . In D2 and D3, a stepwise reduction of the training domain size \bar{r}_{max} (shaded area) and \bar{r}_{weq} (black line) improves each the inference of the ground truth $\bar{p}(\bar{x}, \bar{y}, \bar{t})$ in the vicinity of the well.

$$\tau(\bar{x}, \bar{y}, \bar{t}) = \begin{cases} \frac{(\bar{x} - \bar{x}_{\min})(\bar{x}_{\max} - \bar{x})(\bar{y} - \bar{y}_{\min})(\bar{y}_{\max} - \bar{y})}{0.5^4 \times (\bar{x}_{\max} - \bar{x}_{\min})^2 \times (\bar{y}_{\max} - \bar{y}_{\min})^2} \frac{\bar{t}}{t_{\max}}, & \text{if } |\bar{x}| \leq \bar{x}_{\max}, |\bar{y}| \leq \bar{y}_{\max} \\ 0, & \text{if } |\bar{x}| > \bar{x}_{\max}, |\bar{y}| > \bar{y}_{\max} \end{cases}, \quad (8)$$

where \bar{x}_{\max} and \bar{y}_{\max} are the domain boundaries and \bar{t}_{\max} is the maximum modeling time. $\tau(\bar{x}, \bar{y}, \bar{t})$ ensures that $\hat{p}_c(\bar{x}, \bar{y}, \bar{t}; \theta)$ equals zero at any domain point beyond the domain boundary, as well as at the initial condition. In addition, $\tau(\bar{x}, \bar{y}, \bar{t})$ is sufficiently partially differentiable for our diffusion problem, that is, twice differentiable over \bar{x} and once differentiable over \bar{t} .

As introduced in Section 1, PINNs require a minimum ratio $b > 10\%$, where b is the ratio between the equivalent well radius \bar{r}_{weq} and the domain extension \bar{x}_{\max} . To not only meet this condition, but also ensure correct well representation, we introduce WellPINN, a sequential training approach for a series of PINNs (Figure 1). Here, we minimize \mathcal{L} stepwise by training each subsequent PINN model on a smaller subdomain, while using the output of the previously trained PINNs as the initial solution for the near field of the well, by adapting the approach of Wang and Lai (2024). For each training step D , we calculate the equivalent well radius as

$$\bar{r}_{\text{weq}} = b^D \bar{x}_{\max,D}, \quad (9)$$

where we observe optimal regression results for $b = 0.17$ (see Section 4). We set the subdomain size of each subsequent step to the equivalent radius of the previous step as $\bar{x}_{\max,D} =$

$\bar{r}_{\text{weq},D-1}$ (see Figure 1c). The total number of subdomains N is defined as

$$N > \frac{\log\left(\frac{\bar{r}_w}{\bar{x}_{\max}}\right)}{\log(b)}, \quad N \in \mathbb{N}, \quad (10)$$

where \bar{r}_w is the radius of the real well. We calculate the standard deviation for Equation (5) as

$$\sigma_D = \frac{|\bar{r}_{\text{weq}} - \mu_r|}{\sqrt{-2 \ln(\beta)}}, \quad (11)$$

where $\beta = 10^{-2}$ is the target amplitude of the source function that defines \bar{r}_{weq} .

Each pressure solution $\hat{p}_{c,D}$ is composed of all previously trained PINN outputs as

$$\hat{p}_{c,D}(\bar{x}, \bar{y}, \bar{t}; \theta_D) = \sum_{n=1}^D \epsilon_n \times \tau_n(\bar{x}, \bar{y}, \bar{t}) \times \hat{p}_n(\bar{x}, \bar{y}, \bar{t}; \theta_n), \quad (12)$$

where ϵ_n is a specific weighting factor (Wang and Lai, 2024). We assume $\epsilon_D = 1$ at the initialization of the model and update the domain boundaries in $\tau_D(\bar{x}, \bar{y}, \bar{t})$ for each step. As illustrated in Figure 1b and Figure 1c, training begins with the outer domain, where $\hat{p}_{c,1}$ approximates the far field. To correct deviations near \bar{r}_{weq} , the residuals of previous steps are minimized in the following training loss, similar to the multistage PINN training of Wang and Lai (2024).

Using the complete composite solution \hat{p}_c in the PDE residual would require evaluating all PINNs at each epoch. Since only the current network is trainable and the prior ones remain fixed, we reduce the computational cost by isolating the terms of each $\hat{p}_{c,D}$ and incorporating residuals from earlier stages R_n as precomputed terms

$$\mathcal{L}_D = \text{RMSE} \left(\epsilon_D \frac{\bar{\partial} \hat{p}_{c,D}}{\bar{\partial} \bar{t}} - \epsilon_D \overline{\text{div}} (\overline{\text{grad}} \hat{p}_{c,D}) - \bar{f} + \sum_{n=1}^{D-1} R_n \right), \quad (13)$$

where $\sum_{n=1}^{D-1} R_n$ is computed at the beginning of each training stage D . For an optimal scaling of the serial modeling steps, we update the specific weighting factor ϵ_I at the beginning of each subsequent training step as

$$\epsilon_I = \text{Mean} \left| \frac{\bar{f} - \sum_{n=1}^{I-1} R_n}{\bar{\partial} \hat{p}_I / \bar{\partial} \bar{t} - \overline{\text{div}} (\overline{\text{grad}} \hat{p}_I)} \right|, \quad (14)$$

where \hat{p} is the yet untrained network of the respective subdomain. A full derivation of Equation (13) and Equation (14) is provided in Supplementary Information S1. The Training is performed sequentially using the Adam optimizer followed by L-BFGS (Kingma and Ba, 2015; Liu and Nocedal, 1989). We summarize our training workflow Algorithm 1.

Algorithm 1: Sequential PINN Training for Accurate Well Representation

Calculate the minimum number of subdomains $N > \log \left(\frac{\bar{r}_w}{\bar{x}_{\max}} \right) / \log(b)$, $N \in \mathbb{N}$

for $D = 1, 2, \dots, N$ **do**

if $D = 1$ **then**

$\bar{x}_{\max,D} = \bar{x}_{\max}$;

else

$\bar{x}_{\max,D} = \bar{r}_{\text{weq},D-1}$

 Compute equivalent well radius \bar{r}_{weq} from Equation (9)

 Compute standard deviation of the equivalent well σ_D from Equation (11)

 Generate collocation points within subdomain in the boundaries of

$\bar{x}_{\min,D} < \bar{x} < \bar{x}_{\max,D}$ and $\bar{y}_{\min,D} < \bar{y} < \bar{y}_{\max,D}$.

 Construct hard constraint function $\tau_D(\bar{x}, \bar{y}, \bar{t})$ from Equation (8)

 Construct composite solution assuming $\epsilon_D = 1$ from Equation (12)

 Update weighting factor for current training step ϵ_D according to Equation (14).

 Construct residual loss \mathcal{L}_D as in Equation (13).

 Train network $\hat{p}_{c,D}(\bar{x}, \bar{y}, \bar{t}; \theta_D)$ by updating θ_D using the Adam optimizer

 Update weighting factor ϵ_D

 Fine-tune $\hat{p}_{c,D}(\bar{x}, \bar{y}, \bar{t}; \theta_D)$ by updating θ_D using the L-BFGS optimizer

Output: Composite solution of fluid pressure as in Equation (12)

3 Case Study for a 2D PINN with a Single Well

Data Generation with a Numerical Model: We construct a synthetic training dataset by solving Equation (1) with the OpenGeoSys numerical solver (Naumov et al., 2022). We define a two-dimensional domain with the extensions of $-50 \text{ m} < x < 50 \text{ m}$ and $-50 \text{ m} < y < 50 \text{ m}$. We inject at a rate of $q_w = 9.9 \times 10^{-7} \text{ m}^3 \text{ s}^{-1} \text{ m}^{-1}$ in a well with a radius of $\bar{r}_w = 1 \times 10^{-1} \text{ m}$ in the center of the domain. For all boundaries and for the initial condition boundaries, we define a Dirichlet boundary condition with $p = 0 \text{ MPa}$. The material parameters are assumed for a granite-like material with a homogeneous permeability distribution. The PINN has an architecture of $4 \times [40]$ (4 layers, each layer has 40 neurons) with \tanh activation functions, and we train each PINN model for 24 000 training epochs. We provide a table with all material parameters and with the detailed parameterization of our PINN model in Table 1. We run our PINN model on an NVIDIA RTX A4500 GPU. The training times for our three models are 696 s, 1 317 s and 1 801 s, respectively.

Modeling Results: To demonstrate that our model fulfills the requirements outlined in Section 1 for exact well representation, we present a detailed training visualizations in Figure 2 with the first three rows showing the results from the three sequential PINN models. The third and fourth columns show the absolute error $\text{AE}(\bar{x}, 0, \bar{t})$ and the residual $\text{AR}(\bar{x}, 0, \bar{t})$, respectively. The fourth row shows the training and validation loss for the three domains.

In the initial training stage D1 (Figure 2, row one), the cross section in Figure 2a indicates a strong agreement across most of the domain. However, $\hat{p}_{c,D1}$ deviates from \bar{p} within the equivalent well. In particular, early timesteps ($\bar{t} = 0.2$ and $\bar{t} = 35$) are not captured, as their diffusion fronts lie within \bar{r}_{weq} . As shown in Figure 2c, the AE remains below 0.02 in most areas, but rises to 0.53 for $\bar{x} < 9$. The absolute residual (AR) in Figure 2d mirrors this trend, as it remains below 1×10^{-4} in the far field, but increases abruptly within \bar{r}_w , indicating difficulty in capturing the steep gradient of the source term at the well boundary. During D1, we therefore encounter two effects: a mismatch in the vicinity of the well and a mismatch for early timesteps. Both effects motivate our study to pursue the sequential training approach with a stepwise reduction of \bar{r}_{weq} .

In training stage D2, the subdomain shrinks to the extent of the equivalent well of stage D1. Here, the cross sections (Figure 2e and Figure 2f) show an improved fit near \bar{r}_w , and Figure 2g reveals that AE_{max} is reduced by half to 0.25. However, residual discrepancies remain within \bar{r}_{weq} , especially at the source boundary (Figure 2h). D3 further reduces \bar{r}_{weq} towards \bar{r}_w , nearly eliminating the mismatch, as shown in Figure 2i and Figure 2j. Here, even early timesteps are captured, with the mean absolute error (MAE) reduced to 1.02×10^{-2} and AE_{max} being reduced from the initial 0.53 in D1 to 0.11 in D3. Similarly, the maximum value of AR reduces from 1.1×10^1 in D1 to 3.1×10^{-1} in D3.

The loss evolution provides further information about the model training (Figure 2m). Each stage comprises 24 000 epochs (Adam: 20 000, L-BFGS: 4 000). Training loss decreases in D1 from 1×10^{-1} to 1×10^{-4} . For the second training stage, we focus the training on the subdomain with the highest AE and highest AR values, resulting in an initially higher training loss in D2 with 7×10^{-1} , which reduces to 1×10^{-3} . Similarly, training step D3 is initialized with large loss values, namely 3×10^1 , which is reduced by two orders of magnitude to 9×10^{-2} . A divergence between training and validation loss appears in D3 during Adam optimization but resolves during L-BFGS. In total, the results for the application example in Figure 2 show a satisfactory regression result, which implies that our sequential training is able to reduce the significant pressure mismatch of $\text{AE}_{\text{max}} = 0.53$ to $\text{AE}_{\text{max}} = 0.11$ throughout the injection time during two additional training iterations.

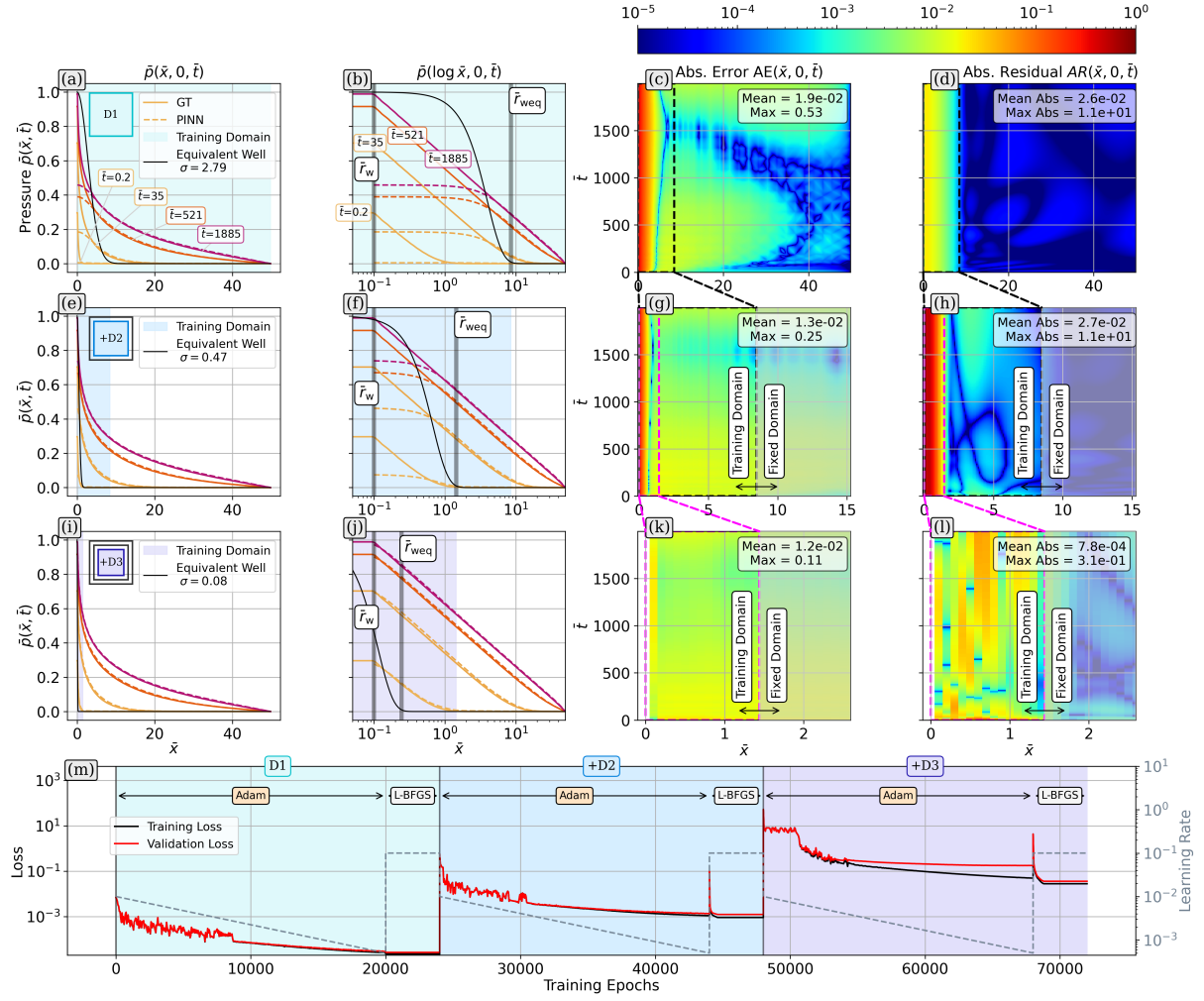


Figure 2 Modeling results of PINN model for transient fluid pressure diffusion with a single well in a 2D domain at the cross section of $\bar{y} = 0$. (a,e,i) Comparison of the ground truth $\bar{p}(\bar{x}, 0, \bar{t})$ versus the PINN output $\hat{p}_{c,D}(\bar{x}, 0, \bar{t}; \theta_D)$ for timesteps $\bar{t} = [0.2, 35, 521, 1885]$ for a linear \bar{x} for the modeling steps D1, D2 and D3, respectively. (b,f,j) scale \bar{x} in log, where the real well radius \bar{r}_w and equivalent radius \bar{r}_{weq} are indicated. (c,g,k) Absolute error $AE(\bar{x}, 0, \bar{t})$ for D1,D2, and D3 with a zoom towards the training domains for D2 and D3. (d,h,l) Absolute Residual $AR(\bar{x}, 0, \bar{t})$ for D1,D2, and D3 with a zoom towards the training domains for D2 and D3. (m) Evolution of training loss and validation loss for D1, D2, and D3.

To further assess the inference of the well pressure, we plot the evolution of the pressure at different distances from the center of the domain \bar{r} (Figure 3a). The PINN model matches the ground truth sufficiently at \bar{r}_w , with only minor deviations throughout injection time. Similar precision is seen at $\bar{r} = 1.0$ and 10.0 , although slight mismatches occur until $\bar{t} = 500$. At the boundary $\bar{r} = 49$, the model infers the boundary condition nearly perfectly due to the hard constraint function τ . We also visualize 2D surface maps for early time $\bar{t} = 0.2$ (Figure 3b–d) and near-stationary state at $\bar{t} = 1000$ (Figure 3e–g). At $\bar{t} = 0.2$, the PINN model accurately captures the pressure front, while it slightly overestimates $\bar{p}(\bar{x}, \bar{y}, \bar{t})$ outside of the front, as illustrated by the AE map in Figure 2d with a range of $0.001 < AE < 0.02$. At later times, discrepancies are most prominent at the domain corners, where $\bar{p}(\bar{x}, \bar{y}, \bar{t})$ spreads non-radially while $\hat{p}_c(\bar{x}, \bar{y}, \bar{t}; \theta)$ remains rather radially shaped, leading to $AE_{\max} = 0.015$. In general, our PINN workflow achieves high accuracy, resolving the well with a ratio of $b = 0.17\%$ per subdomain.

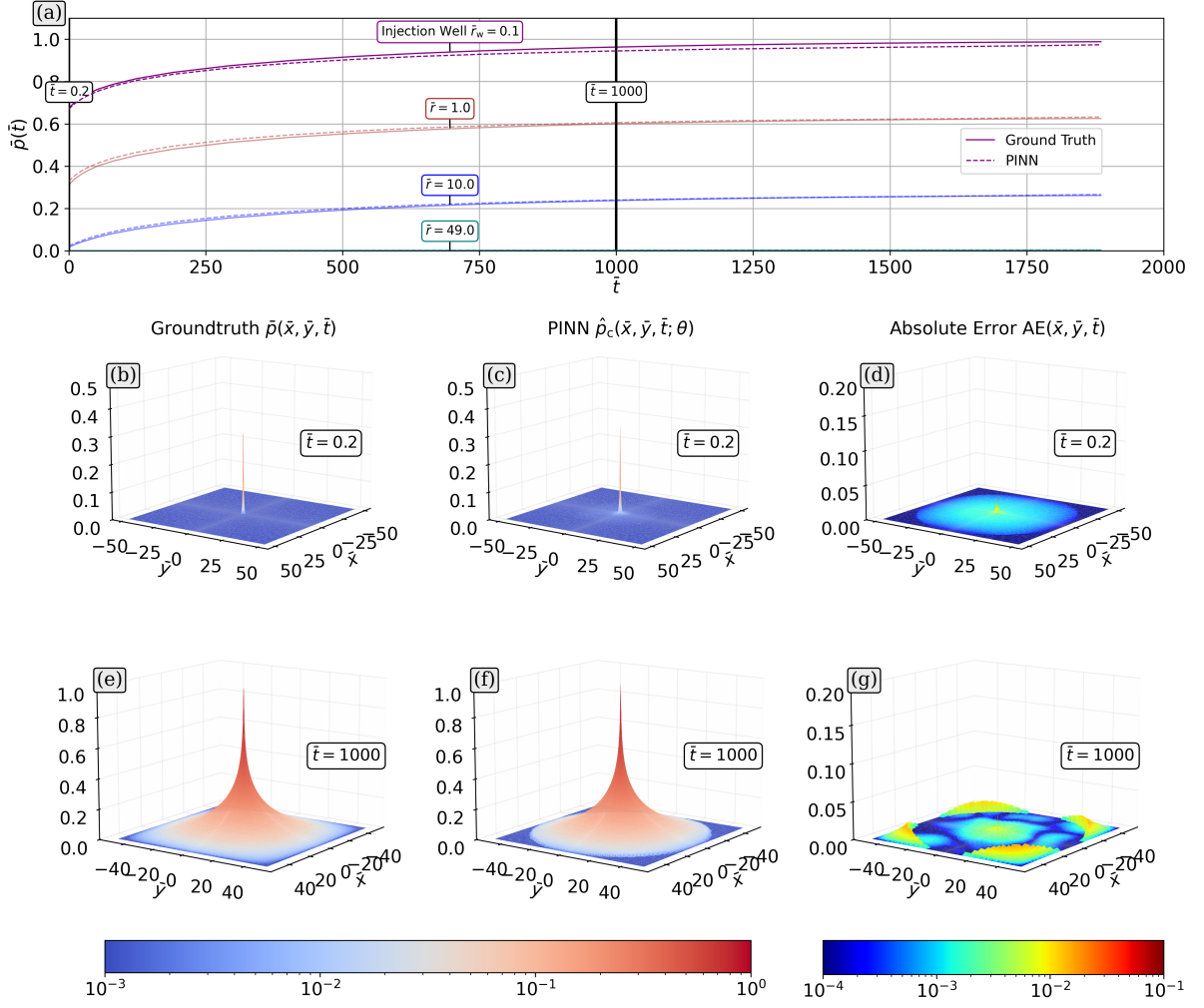


Figure 3 Pressure evolution at the well over the whole modeling domain. (a) Comparison of ground truth $\bar{p}(\bar{x}, \bar{y}, \bar{t})$ and PINN output $\hat{p}_c(\bar{x}, \bar{y}, \bar{t}; \theta)$ over the injection time for the radii $\bar{r} = [0.1, 1.0, 10, 49]$. (b,c,d) 3D surfaces of $\bar{p}(\bar{x}, \bar{y}, \bar{t})$, $\hat{p}_c(\bar{x}, \bar{y}, \bar{t}; \theta)$ and $AE(\bar{x}, \bar{y}, \bar{t})$ for early time at $\bar{t} = 0.2$, respectively. (e,f,g) 3D surfaces of $\bar{p}(\bar{x}, \bar{y}, \bar{t})$, $\hat{p}_c(\bar{x}, \bar{y}, \bar{t}; \theta)$ and $AE(\bar{x}, \bar{y}, \bar{t})$ for late time at $\bar{t} = 1000$, respectively.

4 Discussion

The results demonstrate the optimal representation of the well in $b = 0.17 = \bar{r}_{\text{weq}}/\bar{x}_{\text{max}}$ (Section 3). To quantify the choice of b , we conduct a parameter study for $0.04 < b < 0.22$ (Figure 4), with five realizations per value of b . We analyze the mean and the confidence interval for the mean absolute error on the well (MAE_w), as well as the mean absolute error (MAE_d), and the mean squared residual in the modeling domain (MSR_d). All three metrics show optimal accuracy for $0.1 < b < 0.17$. For $b < 0.1$, the increase of the maximum gradients in the source term in combination with the shrinking area of the equivalent well led to a worsening performance for all metrics (compare Figure 4a, Figure 4b and Supplementary Information S3). Adding more collocation points on the equivalent well has just a limited effect on reducing these errors, because the activation functions are not optimized for such a multi-scale problem. Interestingly, MSR_d decreases at $b = 0.04$, probably due to the optimizer ignoring a negligible source. For $b > 0.06$, the residual MSR_d constantly decreases, confirming that a PINN model with wider \bar{r}_{weq} converges more easily. For $b > 0.17$, MAE_w increases as \bar{r}_{weq} no longer overlaps well with \bar{r}_w , also indicating that a fourth subdomain could solve this problem.

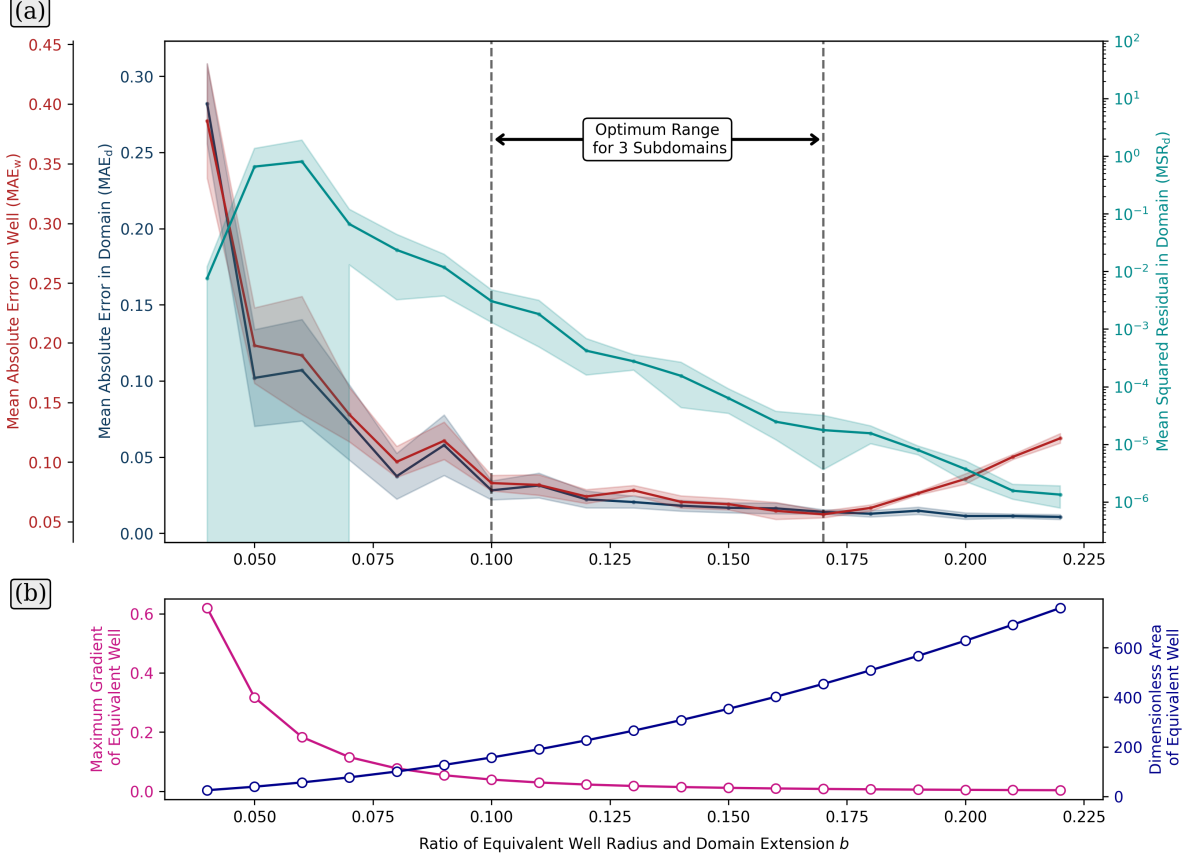


Figure 4 Parameter study for the well representation performance of the PINN model for the equivalent well ratio b . (a) The mean absolute error is given for the well surface as MAE_w (dark red) and for the modeling domain as MAE_d (dark blue) and the mean squared residual MSR_d is also given for the modeling domain. We plot the mean (solid line) and the confidence interval (shaded area) for each metric. The optimum parameter range for having three subdomains is $0.1 < b < 0.17$. (b) Evolution of the maximum gradient and the dimensionless area of the equivalent well function in dependency of b , respectively.

Our study finds that using a PINN model to represent a centimeter-scale pumping well in a reservoir-sized domain requires domain decomposition. Here, we propose a workflow that hard constraints the PINN output at the subdomain boundaries in combination with a sequential training towards the well. This setup improves model training by using only one loss term per PINN, while most importantly, it ensures strict continuity of the composite PINN function, unlike classical approaches which are more suitable for steep jumps at material boundaries (Shukla et al., 2021). In our study, we avoided the use of observational data for $\bar{p}(\bar{x}, \bar{y}, \bar{t})$ to demonstrate that our model infers the fluid pressure from physics alone. However, a data loss term can be easily added, although an appropriate loss term weighting would be beneficial to obtain optimal results (Wang, Sankaran, et al., 2023; Wang and Lai, 2024). Furthermore, we find that logarithmic scaling of input time enhances early-time regression accuracy, a technique not previously applied to well representation in PINNs.

Compared to previous studies, our investigated value $b = 0.17$ for the ratio of the equivalent well radius to the domain extension aligns with the experience in the literature showing $0.1 < b < 0.2$. Several previous studies enhanced model complexity with multiple wells (Liu, Li, et al., 2024; Zhang et al., 2022), heterogeneous domains (Zhang et al., 2022), or compared model performance for various equivalent well functions (Cuomo et al., 2023), achieving reasonable inference of $\bar{p}(\bar{x}, \bar{y}, \bar{t})$ for the far field and for late time steps. We advance this current state-of-the-art with our WellPINN workflow (Section 2) that infers $\bar{p}(\bar{x}, \bar{y}, \bar{t})$ in the vicinity of the well, proven in the exemplary case study in Section 3, and our parameter study for feasible

b values in Section 4. Therefore, we provide an essential step for developing PINNs as versatile reservoir simulators for forward and inverse modeling. Although we test the application of WellPINN solely for a single injection well and constant permeability, we are confident that our workflow is extendable to a heterogeneous permeability field. For adding multiple wells, our current approach of a sequential training for each well might become computationally expensive. Instead of decomposing the domain for each well, future investigations could test sequential training with a stepwise reduced \bar{r}_{weq} and a frequency scaling factor for the activation functions in each $\hat{p}_{\text{c,D}}(\bar{x}, \bar{y}, \bar{t}; \theta_D)$, as proposed by Wang and Lai (2024) for high-frequency domains. Another alternative would be to adapt the ‘hp-VPINN’-method of Kharazmi et al. (2021) for this purpose. Although this multi-well modeling might require more investigation, we are confident that the inverse modeling, namely the determination of k_{mean} by matching p_w and q_w in the Darcy equation, is straightforwardly achievable with our WellPINN workflow.

5 Conclusions

Accurately representing wells remains a key challenge in reservoir modeling, particularly for history matching of flow rate and well pressure during well tests. Although PINNs are becoming increasingly popular for these applications, existing studies have not yet explored how to reliably infer the entire fluid pressure field for a given flow rate. To close this gap, we propose the WellPINN workflow, a sequential PINN-based algorithm that decomposes the modeling domain and trains progressively from the far field toward the near field of the well. Each PINN is trained with a decreasing equivalent well radius \bar{r}_{weq} , using the previous solution as initialization. Continuity of the composite PINN solution is achieved by hard constraining each PINN at the subdomain boundary. This approach results in a final equivalent well radius that matches the real well radius. In our case study, three PINNs are combined to model a well of $r_w = 10$ cm in a domain of $x_{\text{max}} = 50$ m, while scaling time logarithmically. Our results demonstrate that WellPINN enables an accurate inference of p_w , including at the early time after the start of injection. Our parameter study identifies $b = 0.17$ as the optimal ratio between the equivalent well radius $\bar{r}_{\text{weq},D}$ and the subdomain extension $\bar{x}_{\text{max},D}$. This result quantifies a trend noted in the literature: centimeter-scale wells cannot be resolved within large domains using a single PINN with standard tanh activation functions. Although further development is needed to optimize our WellPINN workflow for multiwell configurations, our study marks a relevant step toward establishing PINNs as a flexible reservoir simulator for the field of subsurface flow modeling.

6 CRediT authorship contribution statement

Linus Walter: Conceptualization, Formal analysis, Investigation, Methodology, Software, Visualization, Writing – original draft. **Qingkai Kong:** Methodology, Software, Supervision, Writing – review & editing. **Sara Hanson-Hedgecock:** Supervision, Writing – review & editing. **Víctor Vilarrasa:** Conceptualization, Funding acquisition, Methodology, Project administration, Resources, Supervision, Writing – review & editing

Open Research Section

We generate our data using the OpenGeoSys (OGS) version 6.4.3 open source code by Naumov et al. (2022) available at <https://www.opengeosys.org/>. The PINN model is based on the pytorch version 2.3.1 of Adam Paszke et al. (2024) openly available at <https://pytorch.org/>. Our sampling method for the collocation points is inspired by the SciANN Python package of Haghighat and Juanes (2021). We created all figures with Matplotlib version 3.9.1 (Hunter, 2007; Team, 2024), available under the Matplotlib license at <https://matplotlib.org/>. All

data sets are produced with numpy version 2.0.0 by Harris et al. (2020) available at <https://pypi.org/project/numpy/> and with pandas version 2.2.2 by The pandas development team (2024) available at <https://pandas.pydata.org/>.

The input data includes the configuration file and the mesh for the numerical model as well as the output of the OGS model as a plain text file in CSV format. All relevant input data and Python code necessary to reproduce our results are licensed under the GNU General Public License 3 or later (GPL-3.0). and will be made openly available at <https://github.com/linuswaller/WellPINN> following the journal publication of this manuscript.

Acknowledgments

LW, SHH and VV acknowledge funding from the European Research Council (ERC) under the European Union's Horizon 2020 Research and Innovation Program through the Starting Grant GEO-REST (www.georest.eu) under Grant Agreement No. 801809. IMEDEA is an accredited "Maria de Maeztu Excellence Unit" (Grant CEX2021-001198, funded by MICIU/AEI/10.13039/501100011033). The work of QK is under the auspices of the US Department of Energy by Lawrence Livermore National Laboratory under contract DE-AC52 07NA27344. This paper is published under LLNL-JRNL-2006105. We also express our gratitude to our collaborator Francesco Parisio for his contributions to the conceptualization of this project.

References

- Abbasi, J., & Andersen, P. Ø. (2023). Physical Activation Functions (PAFs): An Approach for More Efficient Induction of Physics into Physics-Informed Neural Networks (PINNs), 26. DOI: <https://doi.org/10.48550/arXiv.2205.14630>.
- Abbasi, J., Moseley, B., Kurotori, T., Jagtap, A. D., Kovscek, A. R., Hiorth, A., & Østebø Andersen, P. (2025). History-Matching of imbibition flow in fractured porous media Using Physics-Informed Neural Networks (PINNs). *Computer Methods in Applied Mechanics and Engineering*, 437, 117784. DOI: <https://doi.org/10.1016/j.cma.2025.117784>.
- Adam Paszke, Sam Gross, Francisco Massa, Adam Lerer, James Bradbury, Gregory Chanan, Trevor Killeen, Zeming Lin, Natalia Gimelshein, Luca Antiga, Alban Desmaison, Andreas Köpf, Edward Yang, Zach DeVito, Martin Raison, Alykhan Tejani, Sasank Chilamkurthy, Benoit Steiner, Lu Fang, ... Soumith Chintala. (2024). PyTorch: An Imperative Style, High-Performance Deep Learning Library. URL: <https://github.com/pytorch/pytorch/releases/tag/v2.3>.
- Baydin, A. G., Pearlmutter, B. A., Radul, A. A., & Siskind, J. M. (2015). Automatic differentiation in machine learning: A survey. DOI: <https://doi.org/10.48550/ARXIV.1502.05767>.
- Beckers, K. F., & McCabe, K. (2019). GEOPHIRES v2.0: Updated geothermal techno-economic simulation tool. *Geothermal Energy*, 7(1), 5. DOI: <https://doi.org/10.1186/s40517-019-0119-6>.
- Bentley, M. (2020). Reservoir Modeling and Simulation. In R. Sorkhabi (Ed.), *Encyclopedia of Petroleum Geoscience* (pp. 1–13). Springer International Publishing. DOI: https://doi.org/10.1007/978-3-319-02330-4_233-1.
- Castelletto, N., Corbett, B., Cremon, M., Fu, P., Gross, H., Hamon, F., Huang, J., Klevtsov, S., Lapene, A., Mazuyer, A., Semnani, S., Settgast, R., Sherman, C., Vargas, A., White, J. A., & White, C. (2024). GEOS simulation framework. URL: <https://github.com/libgeos/geos>.
- Cuomo, S., De Rosa, M., Giampaolo, F., Izzo, S., & Schiano Di Cola, V. (2023). Solving ground-water flow equation using physics-informed neural networks. *Computers & Mathematics with Applications*, 145, 106–123. DOI: <https://doi.org/10.1016/j.camwa.2023.05.036>.

- Giudicelli, G., Lindsay, A., Harbour, L., Icenhour, C., Li, M., Hansel, J. E., German, P., Behne, P., Marin, O., Stogner, R. H., Miller, J. M., Schwen, D., Wang, Y., Munday, L., Schunert, S., Spencer, B. W., Yushu, D., Recuero, A., Prince, Z. M., . . . Permann, C. (2024). 3.0 - MOOSE: Enabling massively parallel multiphysics simulations. *SoftwareX*, 26, 101690. DOI: <https://doi.org/10.1016/j.softx.2024.101690>.
- Haghighat, E., Amini, D., & Juanes, R. (2021). Physics-informed neural network simulation of multiphase poroelasticity using stress-split sequential training. *arXiv:2110.03049 [cs]*. DOI: <https://doi.org/10.1016/j.cma.2022.115141>.
- Haghighat, E., & Juanes, R. (2021). SciANN: A Keras/TensorFlow wrapper for scientific computations and physics-informed deep learning using artificial neural networks [Software]. *Computer Methods in Applied Mechanics and Engineering*, 373. DOI: <https://doi.org/10.1016/j.cma.2020.113552>.
- Hanna, J. M., Aguado, J. V., Comas-Cardona, S., Askri, R., & Borzacchiello, D. (2022). Residual-based adaptivity for two-phase flow simulation in porous media using Physics-informed Neural Networks. *Computer Methods in Applied Mechanics and Engineering*, 396, 115100. DOI: <https://doi.org/10.1016/j.cma.2022.115100>.
- Harris, C. R., Millman, K. J., Van Der Walt, S. J., Gommers, R., Virtanen, P., Cournapeau, D., Wieser, E., Taylor, J., Berg, S., Smith, N. J., Kern, R., Picus, M., Hoyer, S., Van Kerkwijk, M. H., Brett, M., Haldane, A., Del Río, J. F., Wiebe, M., Peterson, P., . . . Oliphant, T. E. (2020). Array programming with NumPy. *Nature*, 585(7825), 357–362. DOI: <https://doi.org/10.1038/s41586-020-2649-2>.
- Hölting, B., & Coldewey, W. G. (2013). *Hydrogeologie* (Vol. 66). Spektrum Akademischer Verlag. DOI: <https://doi.org/10.1007/978-3-8274-2354-2>.
- Huang, X., Liu, H., Shi, B., Wang, Z., Yang, K., Li, Y., Weng, B., Wang, M., Chu, H., Zhou, J., Yu, F., Hua, B., Chen, L., & Dong, B. (2021). Solving Partial Differential Equations with Point Source Based on Physics-Informed Neural Networks. URL: <http://arxiv.org/abs/2111.01394>.
- Huang, X., & Alkhalifah, T. (2023). GaborPINN: Efficient Physics-Informed Neural Networks Using Multiplicative Filtered Networks. *IEEE Geoscience and Remote Sensing Letters*, 20, 1–5. DOI: <https://doi.org/10.1109/LGRS.2023.3330774>.
- Hunter, J. D. (2007). Matplotlib: A 2D Graphics Environment [Software]. *Computing in Science & Engineering*, 9(3), 90–95. DOI: <https://doi.org/10.1109/MCSE.2007.55>.
- Karniadakis, G. E., Kevrekidis, I. G., Lu, L., Perdikaris, P., Wang, S., & Yang, L. (2021). Physics-informed machine learning. *Nature Reviews Physics*, 3(6), 422–440. DOI: <https://doi.org/10.1038/s42254-021-00314-5>.
- Karpatne, A., Atluri, G., Faghmous, J. H., Steinbach, M., Banerjee, A., Ganguly, A., Shekhar, S., Samatova, N., & Kumar, V. (2017). Theory-Guided Data Science: A New Paradigm for Scientific Discovery from Data. *IEEE Transactions on Knowledge and Data Engineering*, 29(10), 2318–2331. DOI: <https://doi.org/10.1109/TKDE.2017.2720168>.
- Kharazmi, E., Zhang, Z., & Karniadakis, G. E. (2021). Hp-VPINNs: Variational physics-informed neural networks with domain decomposition. *Computer Methods in Applied Mechanics and Engineering*, 374, 1–21. DOI: <https://doi.org/10.1016/j.cma.2020.113547>.
- Kingma, D. P., & Ba, J. L. (2015). Adam: A method for stochastic optimization. *3rd International Conference on Learning Representations, ICLR 2015 - Conference Track Proceedings*, 1–15.
- Lagaris, I., Likas, A., & Fotiadis, D. (1998). Artificial neural networks for solving ordinary and partial differential equations. *IEEE Transactions on Neural Networks*, 9(5), 987–1000. DOI: <https://doi.org/10.1109/72.712178>.
- Lai, M.-C., Song, Y., Yuan, X., Yue, H., & Zeng, T. (2023). The Hard-Constraint PINNs for Interface Optimal Control Problems. DOI: <https://doi.org/10.48550/ARXIV.2308.06709>. Github: <https://github.com/tianyouzeng/PINNs-interface-optimal-control>.
- Langtangen, H. P., & Pedersen, G. K. (2016). *Scaling of Differential Equations*. Springer International Publishing. DOI: <https://doi.org/10.1007/978-3-319-32726-6>.

- Lehmann, F., Fahs, M., Alhubail, A., & Hoteit, H. (2023). A mixed pressure-velocity formulation to model flow in heterogeneous porous media with physics-informed neural networks. *Advances in Water Resources*, 181, 104564. DOI: <https://doi.org/10.1016/j.advwatres.2023.104564>.
- Liu, A., Li, J., Bi, J., Chen, Z., Wang, Y., Lu, C., Jin, Y., & Lin, B. (2024). A novel reservoir simulation model based on physics informed neural networks. *Physics of Fluids*, 36(11), 116617. DOI: <https://doi.org/10.1063/5.0239376>.
- Liu, D. C., & Nocedal, J. (1989). On the limited memory BFGS method for large scale optimization. *Mathematical Programming*, 45(1-3), 503–528. DOI: <https://doi.org/10.1007/BF01589116>.
- Lu, L., Pestourie, R., Yao, W., Wang, Z., Verdugo, F., & Johnson, S. G. (2021). Physics-Informed Neural Networks with Hard Constraints for Inverse Design. *SIAM Journal on Scientific Computing*, 43(6), B1105–B1132. DOI: <https://doi.org/10.1137/21M1397908>.
- Minsky, M., & Papert, S. (1969). *Perceptrons: An introduction to computational geometry* (2. print. with corr.). The MIT Press.
- Naumov, D., Bilke, L., Fischer, T., Rink, K., Wang, W., Watanabe, N., Lu, R., Grunwald, N., Zill, F., Buchwald, J., Huang, Y., Bathmann, J., Chen, C., Chen, S., Meng, B., Shao, H., Kern, D., Yoshioka, K., Rodriguez, J., ... Ning, Z. (2022). OpenGeoSys [Software]. DOI: <https://doi.org/10.5281/ZENODO.7092676>.
- Olivella, S., Vaunat, J., & Rodriguez-Dono, A. (2023). CODE_BRIGHT. URL: <https://deca.upc.edu/en/projects/c>
- Raissi, M., Perdikaris, P., & Karniadakis, G. E. (2019). Physics-informed neural networks: A deep learning framework for solving forward and inverse problems involving nonlinear partial differential equations. *Journal of Computational Physics*, 378, 686–707. DOI: <https://doi.org/10.1016/j.jcp.2018.10.045>.
- Roy, P., & Castonguay, S. T. (2024). Exact enforcement of temporal continuity in sequential physics-informed neural networks. *Computer Methods in Applied Mechanics and Engineering*, 430, 117197. DOI: <https://doi.org/10.1016/j.cma.2024.117197>.
- Rumelhart, D. E., Hinton, G. E., & Williams, R. J. (1986). Learning representations by back-propagating errors. *Nature*, 323(6088), 533–536. DOI: <https://doi.org/10.1038/323533a0>.
- Sarma, A. K., Roy, S., Annavarapu, C., Roy, P., & Jagannathan, S. (2024). Interface PINNs (I-PINNs): A physics-informed neural networks framework for interface problems. *Computer Methods in Applied Mechanics and Engineering*, 429, 117135. DOI: <https://doi.org/10.1016/j.cma.2024.117135>.
- Shen, C., Appling, A. P., Gentine, P., Bandai, T., Gupta, H., Tartakovsky, A., Baity-Jesi, M., Fencia, F., Kifer, D., Li, L., Liu, X., Ren, W., Zheng, Y., Harman, C. J., Clark, M., Farthing, M., Feng, D., Kumar, P., Aboelyazeed, D., ... Lawson, K. (2023). Differentiable modelling to unify machine learning and physical models for geosciences. *Nature Reviews Earth & Environment*, 4(8), 552–567. DOI: <https://doi.org/10.1038/s43017-023-00450-9>.
- Shukla, K., Jagtap, A. D., & Karniadakis, G. E. (2021). Parallel physics-informed neural networks via domain decomposition. *Journal of Computational Physics*, 447, 110683. DOI: <https://doi.org/10.1016/j.jcp.2021.110683>.
- Slotte, P. A., & Berg, C. F. (2017). *Lecture notes in well-testing* (tech. rep.). NTNU. Trondheim.
- Soriano, M. A., Siegel, H. G., Johnson, N. P., Gutchess, K. M., Xiong, B., Li, Y., Clark, C. J., Plata, D. L., Deziel, N. C., & Saiers, J. E. (2021). Assessment of groundwater well vulnerability to contamination through physics-informed machine learning. *Environmental Research Letters*, 16(8), 084013. DOI: <https://doi.org/10.1088/1748-9326/ac10e0>.
- Sukumar, N., & Srivastava, A. (2022). Exact imposition of boundary conditions with distance functions in physics-informed deep neural networks. *Computer Methods in Applied Mechanics and Engineering*, 389, 114333. DOI: <https://doi.org/10.1016/j.cma.2021.114333>.

- Sun, J., Hu, L., Li, D., Sun, K., & Yang, Z. (2022). Data-driven models for accurate groundwater level prediction and their practical significance in groundwater management. *Journal of Hydrology*, 608, 127630. DOI: <https://doi.org/10.1016/j.jhydrol.2022.127630>.
- Tartakovsky, A. M., Marrero, C. O., Perdikaris, P., Tartakovsky, G. D., & Barajas-Solano, D. (2020). Physics-Informed Deep Neural Networks for Learning Parameters and Constitutive Relationships in Subsurface Flow Problems. *Water Resources Research*, 56(5). DOI: <https://doi.org/10.1029/2019WR026731>.
- Taufik, M. H., Alkhalifah, T., & Waheed, U. B. (2024). Stable neural network-based traveltime tomography using hard-constrained measurements. *GEOPHYSICS*, 89(6), U87–U99. DOI: <https://doi.org/10.1190/geo2024-0040.1>.
- Team, T. M. D. (2024). Matplotlib: Visualization with Python. DOI: <https://doi.org/10.5281/ZENODO.12652732>.
- Teng, Y., Zhang, X., Wang, Z., & Ju, L. (2022). Learning green's functions of linear reaction-diffusion equations with application to fast numerical solver. In B. Dong, Q. Li, L. Wang, & Z.-Q. J. Xu (Eds.), *Proceedings of mathematical and scientific machine learning* (pp. 1–16, Vol. 190). PMLR. URL: <https://proceedings.mlr.press/v190/teng22a.html>.
- The pandas development team. (2024). Pandas-dev/pandas: Pandas. DOI: <https://doi.org/10.5281/ZENODO.10957263>.
- Vaezi, I., Alcolea, A., Meier, P., Parisio, F., Carrera, J., & Vilarrasa, V. (2024). Numerical modeling of hydraulic stimulation of fractured crystalline rock at the bedretto underground laboratory for geosciences and geoenergies. *International Journal of Rock Mechanics and Mining Sciences*.
- Wang, H. F. (2000). *Theory of linear poroelasticity with applications to geomechanics and hydrogeology*. Princeton Univ. Press.
- Wang, N., Kong, X.-Z., & Zhang, D. (2024). Physics-Informed Convolutional Decoder (PICD): A Novel Approach for Direct Inversion of Heterogeneous Subsurface Flow. *Geophysical Research Letters*, 51(13), e2024GL108163. DOI: <https://doi.org/10.1029/2024GL108163>.
- Wang, N., Zhang, D., Chang, H., & Li, H. (2020). Deep learning of subsurface flow via theory-guided neural network. *Journal of Hydrology*, 584(January), 124700. URL: <https://doi.org/10.1016/j.jhydrol.2020.124700>.
- Wang, S., Sankaran, S., Wang, H., & Perdikaris, P. (2023). An Expert's Guide to Training Physics-informed Neural Networks. *Preprint*. DOI: <https://doi.org/10.48550/ARXIV.2308.08468>.
- Wang, Y., & Lai, C.-Y. (2024). Multi-stage neural networks: Function approximator of machine precision. *Journal of Computational Physics*, 504, 112865. DOI: <https://doi.org/10.1016/j.jcp.2024.112865>.
- Watson, A. T., Wade, J. G., & Ewing, R. E. (1994). Parameter and System Identification for Fluid Flow in Underground Reservoirs. In L. Arkeryd, H. Engl, A. Fasano, R. M. M. Mattheij, P. Neittaanmäki, H. Neunzert, H. W. Engl, & J. McLaughlin (Eds.), *Proceedings of the Conference Inverse Problems and Optimal Design in Industry* (pp. 81–108). Vieweg+Teubner Verlag. DOI: https://doi.org/10.1007/978-3-322-96658-2_5.
- Yan, X., Lin, J., Wang, S., Zhang, Z., Liu, P., Sun, S., Yao, J., & Zhang, K. (2024). Physics-Informed Neural Network Simulation of Two-Phase Flow in Heterogeneous and Fractured Porous Media. *Advances in Water Resources*, 104731. DOI: <https://doi.org/10.1016/j.advwatres.2024.104731>.
- Zhang, X., Zhu, Y., Wang, J., Ju, L., Qian, Y., Ye, M., & Yang, J. (2022). GW-PINN: A deep learning algorithm for solving groundwater flow equations. *Advances in Water Resources*, 165, 104243. DOI: <https://doi.org/10.1016/j.advwatres.2022.104243>.

Table 1 Overview of all operational parameters, material parameters of the numerical model and parameters of the PINN model for the 2D reservoir model with a central injection well

	Parameter	Values
Operational Parameters	Volumetric Flow Rate	$q_w = 9.9 \times 10^{-7} \text{ m}^3 \text{ s}^{-1} \text{ m}^{-1}$
Material parameters of the Numerical Model		
Fluid	Dynamic viscosity	$\mu = 1.006 \times 10^{-3} \text{ Pa s}$
	Density	$\varrho_R^f = 998.2 \text{ kg m}^{-3}$
	Compressibility	$\kappa_R^f = 5.0 \times 10^{-10} \text{ Pa}^{-1}$
Solid	Density	$\varrho_R^s = 2690 \text{ kg m}^{-3}$
	Porosity	$\phi = 0.01$
	Biot-Willis coefficient	$\alpha_b = 0.8$
	Compressibility	$\kappa_R^s = 4.89 \times 10^{-11} \text{ Pa}^{-1}$
	Specific storage as pressure formulation	$S'_s = 4.36 \times 10^{-11} \text{ Pa}^{-1}$
	Intrinsic permeability	$k = 1 \times 10^{-16} \text{ m}^2$
Parameters of the PINN	ANN architecture	$4 \times [40]$
	Activation Function	<code>tanh</code>
	Output Activation Function	<code>softplus</code>
	Learning Rate	Exponential reduction from 1×10^{-2} to 5×10^{-4}
	Loss terms	$\mathcal{L}_{\text{PINN}} = \mathcal{L}_{\text{pde}}$
	Nr of Collocation Points	50 000 (see Supplementary Information S2)
	Nr of Observation Points	0
	Optimizer	Adam + L-BFGS
	Training Epochs	24 000 per Training Sequence
	Loss Term Evaluation Metric	RMSE
	Nr of Subdomains	3
	CP Refinement	Radial refinement following power distribution
	Time scaling	logarithmic with injection start at $\bar{t} = 0.01$